# Efficient Monte-Carlo based system modelling for image reconstruction in preclinical pinhole SPECT

Nguyen, Minh Phuong; Goorden, Marlies C.; Ramakers, Ruud M.; Beekman, Freek J.

**DOI**
10.1088/1361-6560/ac0682

**Publication date**
2021

**Document Version**
Final published version

**Published in**
Physics in Medicine and Biology

**Citation (APA)**
Nguyen, M. P., Goorden, M. C., Ramakers, R. M., & Beekman, F. J. (2021). Efficient Monte-Carlo based system modelling for image reconstruction in preclinical pinhole SPECT. *Physics in Medicine and Biology*, *66*(12), Article 125013. https://doi.org/10.1088/1361-6560/ac0682

**PAPER** • **OPEN ACCESS**

# Efficient Monte-Carlo based system modelling for image reconstruction in preclinical pinhole SPECT

To cite this article: Minh Phuong Nguyen *et al* 2021 *Phys. Med. Biol.* **66** 125013

Physics in Medicine & Biology

IPEM Institute of Physics and Engineering in Medicine

OPEN ACCESS

RECEIVED
6 February 2021

REVISED
13 May 2021

ACCEPTED FOR PUBLICATION
28 May 2021

PUBLISHED
16 June 2021



PAPER

# Efficient Monte-Carlo based system modelling for image reconstruction in preclinical pinhole SPECT

**Minh Phuong Nguyen**[1], **Marlies C Goorden**[1], **Ruud M Ramakers**[1,2,3] **and Freek J Beekman**[1,2,3]

[1] Section Biomedical Imaging, Delft University of Technology, Delft, The Netherlands
[2] MILabs B.V., Utrecht, The Netherlands
[3] Department of Translational Neuroscience, Brain Center Rudolf Magnus, University Medical Center Utrecht, The Netherlands

**E-mail:** m.p.nguyen@tudelft.nl

**Keywords:** pinhole, SPECT, ultra-high-resolution, system matrix, Monte-Carlo simulation

## Abstract

The use of multi-pinhole collimation has enabled ultra-high-resolution imaging of SPECT and PET tracers in small animals. Key for obtaining high-quality images is the use of statistical iterative image reconstruction with accurate energy-dependent photon transport modelling through collimator and detector. This can be incorporated in a system matrix that contains the probabilities that a photon emitted from a certain voxel is detected at a specific detector pixel. Here we introduce a fast Monte-Carlo based (FMC-based) matrix generation method for pinhole imaging that is easy to apply to various radionuclides. The method is based on accelerated point source simulations combined with model-based interpolation to straightforwardly change or combine photon energies of the radionuclide of interest. The proposed method was evaluated for a VECTor PET-SPECT system with (i) a HE-UHR-M collimator and (ii) an EXIRAD-3D 3D autoradiography collimator. Both experimental scans with $^{99m}$Tc, $^{111}$In, and $^{123}$I, and simulated scans with $^{67}$Ga and $^{90}$Y were performed for evaluation. FMC was compared with two currently used approaches, one based on a set of point source measurements with $^{99m}$Tc (dubbed traditional method), and the other based on an energy-dependent ray-tracing simulation (ray-tracing method). The reconstruction results show better image quality when using FMC-based matrices than when applying the traditional or ray-tracing matrices in various cases. FMC-based matrices generalise better than the traditional matrices when imaging radionuclides with energies deviating too much from the energy used in the calibration and are computationally more efficient for very-high-resolution imaging than the ray-tracing matrices. In addition, FMC has the advantage of easily combining energies in a single matrix which is relevant when imaging radionuclides with multiple photopeak energies (e.g. $^{67}$Ga and $^{111}$In) or with a continuous energy spectrum (e.g. $^{90}$Y). To conclude, FMC is an efficient, accurate, and versatile tool for creating system matrices for ultra-high-resolution pinhole SPECT.

## 1. Introduction

Statistical iterative image reconstruction is prominently used in SPECT and PET (Hutton *et al* 1997, Qi and Leahy 2006). To obtain high-quality images, accurate knowledge of the energy-dependent photon transport through the collimator and in the detector is required. This is usually captured in the point spread functions (PSFs), the scanner's response to a point source. PSFs for all voxels in the field-of-view (FOV) together can be combined in the so-called system matrix, with matrix elements corresponding to the probability that a photon emitted from a certain voxel is detected in a certain detector pixel. For well representing these probabilities, the PSFs need to be noiseless.

Several methods to obtain the system matrix for pinhole SPECT are in use. They can be grouped into three main categories. The first approach is based on analytical modelling of the scanner with some pre-determined geometrical information obtained from a calibration measurement (Feng *et al* 2010, Aguiar *et al* 2014,

Bitar *et al* 2014). This method requires a very precise calibration, especially for high-resolution pinhole systems because such systems are susceptible to small parameter variations. The second approach to obtain the system matrix is by directly measuring the PSFs from a tiny radioactive source sequentially placed at many voxel locations. This approach provides accurate system matrices as the measurement accounts for all realistic system geometries and physics processes within the scanner. Some researchers proposed to measure a point source at each of the voxels in the FOV (Liu *et al* 2002, Furenlid *et al* 2004, Hesterman *et al* 2007). However, with the dramatic resolution increase of recent pinhole SPECT systems, the massive number of required measurements often makes this approach infeasible. A practical way is to measure only a small number of PSFs, and then interpolate to estimate the missing PSFs (van der Have *et al* 2008, Miller *et al* 2012). This is time-efficient and has been used in preclinical pinhole SPECT systems to produce both highly quantitative (Wu *et al* 2010) and high-resolution images, currently with resolutions down to 0.12 mm (Nguyen *et al* 2020b). The third approach is to perform Monte-Carlo simulation (MCS) to obtain a full system matrix as proposed in Bitar *et al* (2011), Aguiar *et al* (2014), Auer *et al* (2018). This approach can accurately account for all kinds of physics processes, without the need for extensive measurements assuming that the geometry is exactly known. The drawback is that MCS is computationally demanding; therefore, it is time-consuming and may even be infeasible to obtain noiseless PSFs for very-high-resolution pinhole SPECT.

For pinhole scanners in our labs, U-SPECT (Beekman *et al* 2005, van der Have *et al* 2009) and VECTor (Goorden *et al* 2013), we usually start with a calibration measurement using a $^{99m}$Tc (140 keV) point source placed at a few hundred positions within the FOV to obtain a set of PSFs. Then, a system matrix is traditionally generated by a PSF fitting and an interpolation procedure as described in van der Have *et al* (2008). In this method, the measured point source ideally needs to be smaller than the image voxel, meaning that for very-high-resolution systems like EXIRAD-3D (voxel size 50 $\mu$m), it is challenging to fabricate such a tiny point source still containing a sufficiently high activity. Besides, such a matrix generated from $^{99m}$Tc point source measurements describes photon transport at 140 keV emission energy. It can also be used to reconstruct other radionuclides emitting photons with energies in close proximity to 140 keV such as $^{123}$I (159 keV), but it is sub-optimal to be used in reconstructing radionuclides emitting photons with very different energies. In principle, one could envisage using a separate point source calibration for each radionuclide, but this is costly and time-consuming if many radionuclides are to be used with the scanner. Additionally, for radionuclides that have a short half-life or radionuclides that are difficult to be produced with a sufficiently high activity condensed in the point source, it is very challenging to obtain noiseless PSFs in the calibration measurement.

In our labs, we also developed a ray-tracing matrix generation method that can easily adapt the matrix energy for different radionuclides. It uses the same $^{99m}$Tc point source calibration for geometrical information and then calculates photon transport for every emission-to-detection path through the collimator and detector material. The input collimator can be modelled with either an analytical description or a voxelised volume. The latter is often used because it can represent complex collimator geometries. The ray-tracing matrix is specifically used for positron emitters and other high-energy radionuclides, and it can also be used for low-energy radionuclides. However, the ray-tracing calculation can be too computationally expensive for ultra-high-resolution systems with complex-geometry collimators such as EXIRAD-3D. It is because, for such a system, this calculation currently requires a voxelised volume to represent the collimator accurately, and both the collimator's voxel size and the image's voxel size need to be very small, which increase the matrix generation time. Moreover, multiple ray-tracing matrices at different energies are required for optimal imaging of radionuclides that emit complex energy spectra, such as $^{67}$Ga with multiple photopeak energies or $^{90}$Y with a wide continuous energy spectrum. This is time demanding both when generating the matrix and for image reconstruction.

Here we present an efficient and accurate FMC-based matrix generation method to address the challenges mentioned above. From the same calibration measurement used for existing matrix generation methods, a fast MCS (FMCS) was performed to obtain a set of PSFs for the targeted radionuclide, and the same interpolation method as in van der Have *et al* (2008) was applied to generate a full system matrix. This way, realistic physics processes are included inside the matrix, and matrices for other radionuclides than the one used in the calibration measurement ($^{99m}$Tc) can be easily generated. The FMC-based method can also combine information from multiple energies in a single matrix to save time in both matrix generation and image reconstruction. We validate the proposed FMC-based matrix with both experiments and simulation studies with $^{99m}$Tc, $^{111}$In, $^{123}$I, $^{67}$Ga, and $^{90}$Y.

## 2. Methods

### 2.1. Studied systems and multi-pinhole collimators

The studies in this work were performed on a VECTor imaging system, commercially available via MILabs B.V., Utrecht, the Netherlands. Two collimators were used, a HE-UHR-M collimator for simultaneous *in vivo*

SPECT/PET imaging of mice with submillimeter resolutions down to 0.6 mm for $^{18}$F and 0.4 mm for $^{99m}$Tc (Goorden *et al* 2013, 2020), and an EXIRAD-3D collimator for *ex vivo* SPECT imaging of tissue samples with a resolution of 120 $\mu$m for $^{99m}$Tc (Nguyen *et al* 2019, 2020b). The system uses a triangular detector setup with three large-FOV gamma-cameras, each equipped with a 9.5 mm thick NaI(Tl) crystal and read out by 55 photomultiplier tubes.

The HE-UHR-M collimator uses clustered-pinhole technology (Goorden and Beekman 2010, Goorden *et al* 2013) that effectively collimates high-energy photons without compromising the collimator's FOV. It contains 162 pinholes with a diameter of 0.7 mm and narrow opening angles of 16°–18° that are grouped in clusters of four. The pinholes are placed in such a way that pinhole projection overlapping on the detector is minimised, and there is no pinhole shielding applied outside the collimator.

The EXIRAD-3D collimator has a large pinhole magnification factor that enables high-resolution *ex vivo* imaging of small tissue samples such as a mouse kidney or a mouse thyroid. It contains 87 pinholes with a diameter of 0.15 mm and an opening angle of 26°. A trapezium-hole lead shielding tube is attached outside the collimator's core to prevent pinhole projection overlapping.

### 2.2. Monte-Carlo simulations

MCSs were used to generate sets of PSFs from which FMC-based system matrices were generated (see section 2.3.2). They were also used for simulated scans in this work (sections 2.4.4, 2.4.5) when corresponding experiments were not performed.

Geant4 Application for Tomographic Emission (GATE) (Jan *et al* 2004, 2011) version 8.0 was used on a CentOS 6.6 cluster with 250 processors for the MCS in this work. System geometries consisting of three NaI(Tl) scintillators and a multi-pinhole collimator were both pre-created as STL files in MATLAB R2018b (MathWorks, Natick, MA, USA) where any geometry calibration information arriving from the real system (see section 2.3.1) was already applied before importing it into GATE. This is much easier than applying the calibration information inside GATE. All the scanned phantoms in GATE were created using analytical shapes. Physics processes were defined using the 'emstandard' physics list builder as explained in the GATE documentation. The radioactive sources ($^{67}$Ga, $^{99m}$Tc, $^{111}$In, $^{123}$I) were created with discrete energy spectra retrieved from Chu *et al* (1998). This allows the simulation to include the full radionuclides' emission energy spectra while still being time-efficient as the spectra were pre-defined. Only for $^{90}$Y, the 'fastY90' source (officially released with GATE version 8.0) was used. This source generates photons directly from a pre-calculated bremsstrahlung kernel, rather than simulating the full electron transport of the emitted beta particle, to speed up the simulation. Furthermore, a threshold of 105 keV was set to exclude lower-energy bremsstrahlung photons that are often not used in $^{90}$Y imaging (Dewaraja *et al* 2017, Chun *et al* 2020). The detector's energy resolution and spatial resolution were modelled in the same way as in Nguyen *et al* (2019).

### 2.3. Monte-Carlo based system modelling

The FMC-based system modelling started with a calibration step followed by an FMC-based point source simulation to obtain an initial set of PSFs for the required radionuclide. Subsequently, a complete system matrix was generated with an interpolation process to fill in the matrix elements for the rest of the voxels within the FOV. Details of this procedure are explained below.

#### *2.3.1. Calibration*

A calibration step was necessary to determine the position and orientation of the collimator, and each detector in the real system as manufacturing inaccuracies could result in a geometry that is slightly different from the original design. This step was not necessary for simulated scans because the geometries in the simulation were exactly as designed. The calibration started with the measurement of a series of $^{99m}$Tc point source responses with sources placed at multiple positions inside the collimator's FOV (435 positions for EXIRAD-3D and 679 positions for HE-UHR-M). The number of positions was determined based on the setup in van der Have *et al* (2008). It depends on the ratio between the size of the collimator's FOV and the matrix voxel size. The positions are distributed on a denser grid near the centre of the FOV than the locations further away from the centre, and in general, the grid's unit size is about 10–40 times the voxel size. The number of point source positions could also be a bit smaller or larger than the stated value; however, it should not be too small to keep sufficient sampling in the FOV and not too large to prevent long calibration time. From the scan, a dataset was generated following the procedure in van der Have *et al* (2008), with each entry containing the projection (PSF) location on the detector, and the corresponding pinhole and point source location. The same geometry fitting algorithm as in Goorden *et al* (2016) was then performed to allow for the rigid transformation of the collimator and each detector to minimise the mean squared error between the measured and estimated PSF locations. Results of this fitting were 24 parameters describing the translation (three parameters) and rotation (three Euler angles) of the

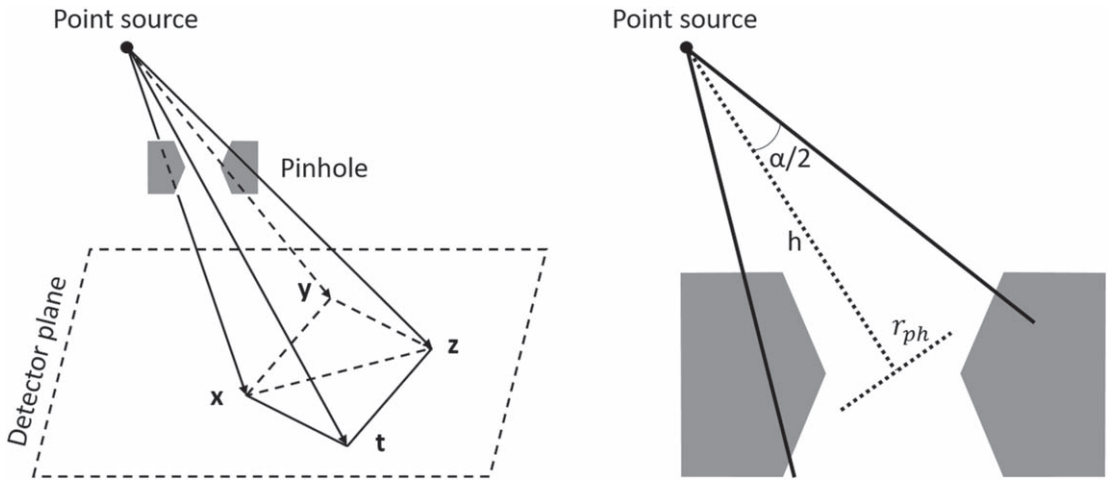


**Figure 1.** Accelerated point source simulation by forced irradiation from the point source to each pinhole.

collimator and each of the three detectors. These parameters were subsequently used to transform the designed collimator and detectors and generate corresponding fitted STL files for the GATE simulation.

*2.3.2. Accelerated point source simulation*

This step is the key that allows for the accurate generation of PSFs for the radionuclide of interest based on MCS without additional measurements. In this simulation, an infinitely small point source was defined in GATE, with the same set of point source positions as in the calibration measurement being used. The point source was assumed to be in water. A simple acceleration technique was applied for the point source simulation by directing the photon emission from the point source to the pinholes in narrow beams instead of the default emission at all angles. This is a kind of forced detection—one of the variance reduction techniques in MCS. There exist several implementations of forced detection for pinhole SPECT (Gieles *et al* 2002, Beenhouwer and Staelens 2010). In our method, only the emission angle from the decay location at the point source is adjusted, and no alteration is applied at individual photon interaction points as in the other methods, meaning it is simple to implement in GATE at the macro level just by setting the span of the polar angle and the azimuthal angle of the emission distribution. Note that this acceleration technique was used for a point source, but it was not suitable for large sources and hence not used for the studied scans in section 2.4.

In our acceleration technique, the photon beams were adapted for each point source and pinhole combination. Each beam formed a regular pyramid with an apex angle defined as (figure 1, equation (1)):

$$\alpha = 2\arctan\left(\frac{r_{ph}\,c}{h}\right), \tag{1}$$

where $r_{ph}$ is the pinhole diameter and $h$ is the distance from the point source to the pinhole centre. The factor $c$ was the same for all point source positions and pinholes in a point source simulation, but it can vary for different radionuclides. It was chosen manually (by checking PSF profiles) to be as small as possible to speed up the simulation while making sure that the beam always covers the entire pinhole and photon penetration and scattering inside the pinhole is not affected.

The pyramid's edges intersect with the detector's surface at four points defined by vectors $\boldsymbol{x}$, $\boldsymbol{y}$, $\boldsymbol{z}$, $\boldsymbol{t}$ from the point source location (figure 1). The solid angle subtended by the detector area seen by the photon beam composed of solid angles of two triangles (Van Oosterom and Strackee 1983):

$$\Omega = 2\arctan\left(\frac{\boldsymbol{x}\cdot(\boldsymbol{y}\times\boldsymbol{z})}{\|\boldsymbol{x}\|\|\boldsymbol{y}\|\|\boldsymbol{z}\| + (\boldsymbol{x}\cdot\boldsymbol{y})\|\boldsymbol{z}\| + (\boldsymbol{x}\cdot\boldsymbol{z})\|\boldsymbol{y}\| + (\boldsymbol{y}\cdot\boldsymbol{z})\|\boldsymbol{x}\|}\right) + 2\arctan\left(\frac{\boldsymbol{x}\cdot(\boldsymbol{z}\times\boldsymbol{t})}{\|\boldsymbol{x}\|\|\boldsymbol{z}\|\|\boldsymbol{t}\| + (\boldsymbol{x}\cdot\boldsymbol{z})\|\boldsymbol{t}\| + (\boldsymbol{x}\cdot\boldsymbol{t})\|\boldsymbol{z}\| + (\boldsymbol{z}\cdot\boldsymbol{t})\|\boldsymbol{x}\|}\right). \tag{2}$$

The number of photon emissions in each beam was $\Omega/4\pi$ times the total number of emissions in $4\pi$. This way, fewer photons needed to be traced, which ultimately resulted in a shorter simulation time. Only for the $^{90}$Y point source simulation, the acceleration technique was not applied because with this radionuclide, the PSF tails were long and a large factor $c$ was needed. As a result, the speed up factor is small, and there is a risk of having overlapping photon beams between different pinholes in a cluster.

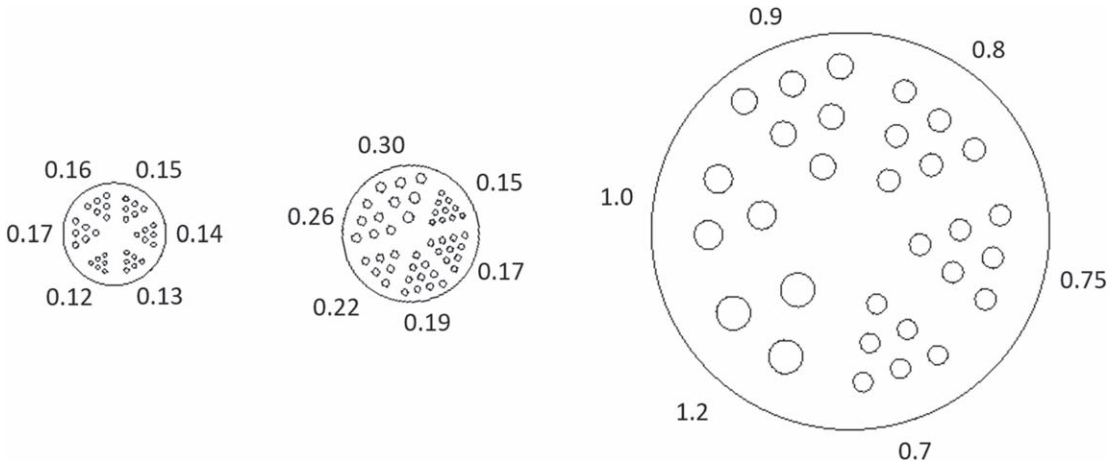


**Figure 2.** Derenzo phantoms with rod diameters indicated in mm. (a) Derenzo phantom 1 with 1.5 mm long hot rods. (b) Derenzo phantom 2 with 2 mm long hot rods. (c) Derenzo phantom 3 with 6 mm long hot rods.

*2.3.3. System matrix generation*

The energy window applied in creating PSFs from the MCS outputs is exactly the same as the energy window applied in creating projection data from the scans (section 2.4). As a result, a single matrix is generated to reconstruct data from a specific energy window setting, no matter whether the projection data is from a single energy window or from multiple energy windows. The obtained PSFs from FMCS were pre-processed to remove high-frequency noise by applying a Richardson–Lucy deconvolution followed by a Gaussian filter with the same kernel, as was also done in van der Have *et al* (2008). The kernel's FWHM was set to be 0.2 mm smaller than the detector's spatial resolution to avoid degrading the PSFs' resolution.

The above step created the PSFs for a small number of point source positions, while the number of required matrix voxels was approximately $2 \times 10^5$ and $2.3 \times 10^3$ times more than that for EXIRAD-3D and HE-UHR-M, respectively. In order to obtain the full set of PSFs for all voxels, the same interpolation method described in van der Have *et al* (2008) was used. This process involved characterising the available PSFs using Gaussian modelling to calculate their location, flux, and width, followed by generalising these parameters over the object space using analytical models. Subsequently, the PSFs at the missing voxel location (not in the scan grid) was created by transforming the nearest available PSF on the detector using the parameters obtained above. As a result, a full system matrix was generated for each radionuclide and each energy window setting and stored on disk. For efficient storage, a cut-off $C$ ($>0$) was applied such that matrix elements that were $>C$% of the maximum were saved.

## 2.4. Studied scans

To evaluate the FMC-based matrix in various situations, complete scans have been performed experimentally or have been simulated using MCS. We used three Derenzo phantoms (figure 2) to assess image resolution, a cylindrical phantom to evaluate image uniformity, and a mouse thyroid scan to demonstrate a real tissue scan. Common SPECT radionuclides $^{99m}$Tc, $^{111}$In, and $^{123}$I as well as two other important radionuclides, $^{67}$Ga and $^{90}$Y, were studied. The scans were performed with EXIRAD-3D, except for the $^{90}$Y scan in section 2.4.5, which was done with the HE-UHR-M collimator because the emission energies of $^{90}$Y were too high for imaging with EXIRAD-3D. The following sections describe the scans in detail.

*2.4.1. Experimental $^{99m}$Tc and $^{111}$In Derenzo phantom scans*

Derenzo phantom 1 having hot rods with diameters ranging from 0.12 to 0.17 mm and a length of 1.5 mm was filled with 4.06 MBq $^{99m}$Tc-pertechnetate and scanned for 3 h at nine bed positions. The rods were in a PMMA disk with a diameter of 8.5 mm and the same length as the rods. The photopeak window was set to 20% at 140 keV.

Derenzo phantom 2 having hot rods with diameters from 0.15 to 0.30 mm and a length of 2 mm was filled with 4.6 MBq $^{111}$In and scanned for 2 h at nine bed positions. The rods were in a PMMA disk with a diameter of 10 mm and the same length as the rods. The photopeak window was set to 20% at 171 keV. Although a 245 keV peak is prominent in the $^{111}$In acquisition energy spectrum, this photopeak was not used because it did not improve the image acquired at 171 keV with EXIRAD-3D.

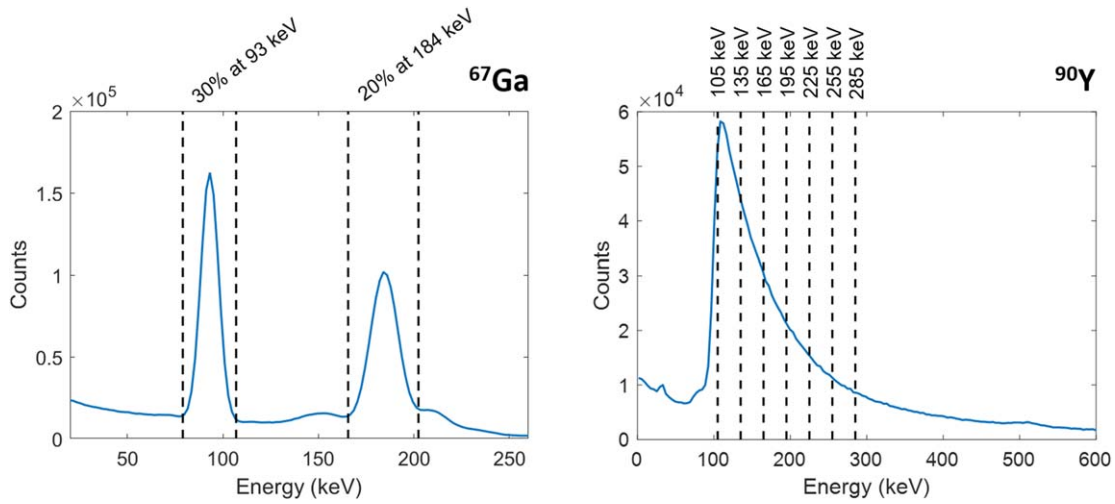


**Figure 3.** The acquisition energy spectra for $^{67}$Ga and $^{90}$Y, obtained from the Derenzo phantom scans for the central bed positions. The dashed lines define the selected energy windows for these scans.

*2.4.2. Experimental $^{99m}$Tc cylindrical phantom scans*

A cylindrical phantom with an inner diameter of 8.5 mm and an inner length of 9.5 mm was filled with 38.6 MBq $^{99m}$Tc-pertechnetate and scanned for 3 h at 128 beds positions. The phantom wall is 1.1 mm thick and made of PMMA. The photopeak window was set to 20% at 140 keV. The images were reconstructed with 100% and 50% of the counts randomly selected from the acquired list-mode data to assess the uniformity for different count levels.

*2.4.3. Experimental $^{123}$I mouse thyroid scan*

A C57BL/6 mouse was used for the thyroid scan, under a protocol approved by the Animal Research Committee at UMC Utrecht and in accordance with the Dutch Law on Animal Experimentation. The mouse was anaesthetised with isoflurane in air and injected intravenously via the tail vein with 10.25 MBq [$^{123}$I]NaI. Four hours post-injection, the mouse was euthanised, and its thyroid was excised and snap-frozen in liquid nitrogen. The thyroid was then placed inside an aluminium holder filled with Tissue-Tek OCT compound (Sakura Finetek Europe, cat. no. 4583) and attached to a cooling unit to keep the tissue frozen throughout the scan. The tissue was scanned for 11 h at four bed positions. The photopeak window was set to 20% at 159 keV.

*2.4.4. Simulated $^{67}$Ga scan: combining multiple photopeaks*

$^{67}$Ga SPECT is commonly used in detecting acute inflammation (Seabold *et al* 1997, Navalkissoor *et al* 2015) and various malignancies such as retroperitoneal fibrosis, lymphomas, cardiac sarcoidosis, and IgG4-related disease (Taki 1990, Kostakoglu *et al* 2002, van Bommel *et al* 2007, Ishii *et al* 2011). The $^{67}$Ga emission spectrum shows several prominent photopeaks (figure 3), including 93 keV with 39.2% abundance, 184 keV with 21.2% abundance, and 300 keV with 16.8% abundance. Usually, the first two photopeaks are used in $^{67}$Ga SPECT either separately or jointly (Moore *et al* 2003, Shirmohammad 2016, Szlávecz *et al* 2019). It is of interest to see the effect of combining these photopeaks in image reconstruction with a single FMC-based matrix that models both energy windows.

Derenzo phantom 1 with hot rods of diameters 0.12–0.17 mm was simulated. The rods were filled with 0.45 MBq $^{67}$Ga and scanned for 16 h with nine bed positions. No material was assumed in the environment surrounding the hot rods. The photopeak window was set to either 30% at 93 keV or 20% at 184 keV. Pre-/post-reconstruction combination of the data from separate energy windows was done as explained in section 2.5.

*2.4.5. Simulated $^{90}$Y scan: utilising a wide continuous energy spectrum*

$^{90}$Y is one of the most commonly used radionuclides for targeted radiotherapies and has been applied in innovative cancer treatments (Lhommel *et al* 2010, Kennedy 2014). Imaging of $^{90}$Y is needed for study and dosimetry to assess doses delivered to lesions and normal tissues. This can be done by either PET or bremsstrahlung SPECT. Although $^{90}$Y decay does not produce gammas, SPECT imaging has been done by utilising bremsstrahlung photons associated with beta emissions. Still, imaging is challenging due to the continuous energy spectrum of the bremsstrahlung photons (figure 3), the low yield of bremsstrahlung photons in tissue, and the range from the beta decay location to the bremsstrahlung emission location. Because of

difficulty in modelling the wide energy spectrum in the system matrix, only a relatively narrow energy window has been used (Siman *et al* 2016). It is desirable to include as many photons as possible by extending the energy window. Recently, several advanced methods have been applied to utilise photons acquired within a wider energy range, e.g. 105–285 or 0–2000 keV, that provide higher quality images than obtained when using a single narrow band (Rong *et al* 2012, Elschot *et al* 2013, Chun *et al* 2020). This was done by having multiple sub-energy windows and energy-dependent matrices, and all of these matrices are used together in image reconstruction.

Here we approached this imaging situation in a different way. By using the FMC-based matrix, 'continuous energy' system modelling can be achieved in a single matrix. Each photon transport was modelled based on the photon energy which can lie anywhere within the selected wide acquisition window. This way, the acquisition window does not need to be separated into sub-bands, and the conventional reconstruction algorithm with a single matrix can be used, which reduces storage for the matrices and shortens reconstruction time.

Derenzo phantom 3 with hot rods of diameters 0.7–1.2 mm was simulated. The rods were filled with 105 MBq $^{90}$Y and scanned for 1.5 h with nine bed positions. The rods were in a water environment—a cylinder with a diameter of 20 mm and a length of 10 mm—because the bremsstrahlung kernel of the 'fastY90' source in GATE was pre-calculated in water. The energy window was set to 105–135 keV, 135–165 keV, 165–195 keV, 195–225 keV, 225–255 keV, or 255–285 keV. Pre-/post-reconstruction combination of the data from separate energy windows was done as explained in section 2.5.

### 2.5. Image reconstruction and evaluation

Images were reconstructed using a similarity-regulated ordered-subset expectation maximisation algorithm (Vaissier *et al* 2016). The voxel size was set to 0.05 mm for EXIRAD-3D and to 0.4 mm for HE-UHR-M. A triple-energy window method was applied to correct for the scatter and background radiation. To this end, two energy windows were placed on both sides of the acquisition window. The side window's width was 20% ($^{99m}$Tc, $^{111}$In, $^{123}$I), 25% ($^{67}$Ga), or 5% ($^{90}$Y) of the acquisition window's width. For $^{90}$Y, the side window was relatively narrow to minimise the effect of the adjacent windows in the continuous energy spectrum. Attenuation correction can be performed for the presented scanners based on the method described in Wu *et al* (2010, 2011). However, for the scans with *ex vivo* and *in vivo* mouse collimators presented in this work, the object attenuation effect is small; therefore, attenuation correction was not performed.

The Derenzo phantom images were evaluated based on the contrast-to-noise ratio (CNR) calculated in the same way as in Walker *et al* (2014) and the system resolution defined as the diameter of the smallest discernible rod. The Derenzo images in the result section were displayed with the iteration number and the Gaussian post-filter size that maximised the CNR averaged over the rod sectors. All of the rod sectors were included in this calculation, except for the experimental $^{111}$In phantom scan, only the three smallest rod sectors were used because with all rod sectors, the obtained image was still too blurry. The cylindrical phantom was reconstructed with 20 iterations and a post-reconstruction 3D Gaussian filter having a FWHM of 0.6 mm was applied. Nine regions of interest (ROIs), each formed by a circular disk with 3 mm radius and 0.3 mm thickness, were evenly placed on the image at 0.45 mm intervals. The uniformity was calculated as the ratio of the standard deviation between the ROIs' means to the average values of the ROIs, and represented as a percentage. The smaller this number is, the more uniform the reconstructed image is. The mouse thyroid images were reconstructed with 20 iterations followed by a 0.15 mm FWHM 3D Gaussian filter and a $3 \times 3 \times 3$ median filter. It was then assessed visually.

The $^{90}$Y beta-to-bremsstrahlung range was corrected in image reconstruction with a pre-calculated kernel which was applied in the forward projection step in reconstruction when using traditional or ray-tracing matrices. This is not required for the FMC-based matrix because this range was already modelled inside the matrix. The beta-to-bremsstrahlung range kernel was obtained from MCS of a $^{90}$Y point source in water.

For the scans where multiple energy windows were available ($^{67}$Ga and $^{90}$Y), the data from these windows were combined in two approaches. In the first approach, projections from separate energy windows were added and reconstructed with one matrix to obtain a *'pre-combined'* image. In the second approach, reconstructed images from separate energy windows were summed to form a *'post-combined'* image.

### 2.6. Comparison with traditional and ray-tracing methods

For all scans in this work, the FMC-based matrices were compared with the matrices generated with the *'traditional'* method (van der Have *et al* 2008) and the *'ray-tracing'* method (Goorden *et al* 2016) that have been commonly used for our nuclear scanners. The traditional matrices were created for 140 keV from a set of $^{99m}$Tc point source measurements and used to reconstruct all radionuclides in this work; therefore, only one matrix is required for each collimator. Note that only for $^{67}$Ga and $^{90}$Y, all data was from simulation; therefore, the point source 'measurements' for the traditional matrices in these cases were also generated with MCS. The ray-tracing matrices were created for the central energies of the selected energy windows; therefore, a new matrix was

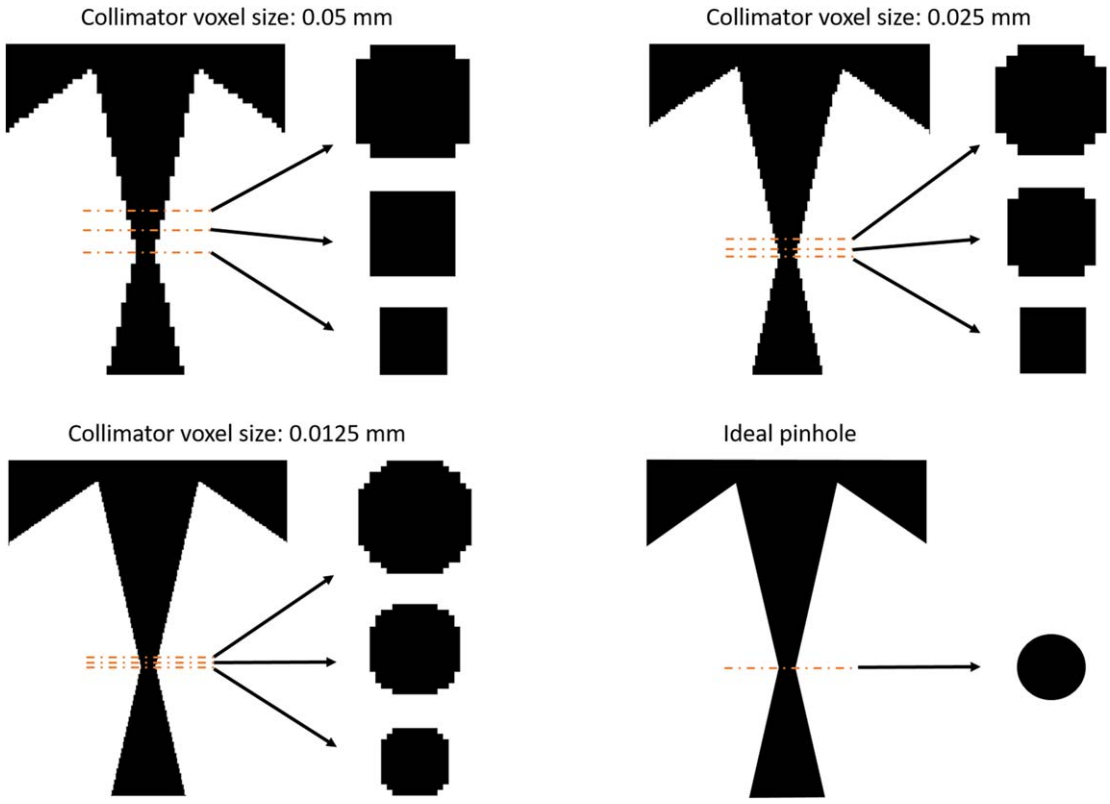


**Figure 4.** Zoom into a pinhole in the EXIRAD-3D collimator used for the ray-tracing matrices to illustrate the accuracy of the voxelised aperture. Black represents air and white represents collimator material. The pinhole diameter is 0.15 mm. The smallest collimator voxel size that was possible to be used in this paper is 0.025 mm.

**Table 1.** The cut-off used for each matrix in this work.

| | EXIRAD-3D | | | | HE-UHR-M |
|---|---|---|---|---|---|
| | $^{99m}$Tc | $^{123}$I | $^{111}$In | $^{67}$Ga | $^{90}$Y |
| Traditional | 20% | 20% | 20% | 0.1% | 0.1% |
| Ray-tracing | 4% | 4% | 4% | 0.1% | 0.1% |
| FMC-based | 4% | 4% | 4% | 0.1% | 0.1% |

**Table 2.** Energy-dependent attenuation coefficient (mm$^{-1}$) in collimator material ($\mu_c$) and in detector crystal ($\mu_d$).that were used for generating ray-tracing matrices which are references to evaluate the FMC-based matrices.

| EXIRAD-3D | | 93 keV | 140 keV | 159 keV | 171 keV | 184 keV | | |
|---|---|---|---|---|---|---|---|---|
| | $\mu_c$ | 9.165 | 3.242 | 2.362 | 1.974 | 1.656 | | |
| | $\mu_d$ | 0.306 | 0.245 | 0.154 | 0.130 | 0.109 | | |
| HE-UHR-M | | 120 keV | 150 keV | 180 keV | 195 keV | 210 keV | 240 keV | 270 keV |
| | $\mu_c$ | 5.132 | 2.914 | 1.861 | 1.538 | 1.293 | 0.957 | 0.744 |
| | $\mu_d$ | 0.258 | 0.175 | 0.115 | 0.094 | 0.082 | 0.061 | 0.047 |

required when changing the radionuclide or energy window setting. For example, for the combined projection data from $^{67}$Ga (93 keV + 184 keV), the ray-tracing matrix was generated for 140 keV (about the mean of these two energies). For the combined projection data from $^{90}$Y (105–285 keV), the matrix was generated for 195 keV. The time necessary to generate matrices with different methods is summarised in table 4.

The matrix cut-off (defined in section 2.3.3) was set as in table 1. For the simulated scans ($^{67}$Ga and $^{90}$Y), the matrix cut-off was always 0.1%. For the experimental scans ($^{99m}$Tc, $^{123}$I, and $^{111}$In), the matrix cut-off was 20% for the traditional matrices and 4% for the other matrices. In principle, the smaller cut-off, the better; however, for the EXIRAD-3D experimental scans, the measured point source size (>100 $\mu$m) was larger than the matrix

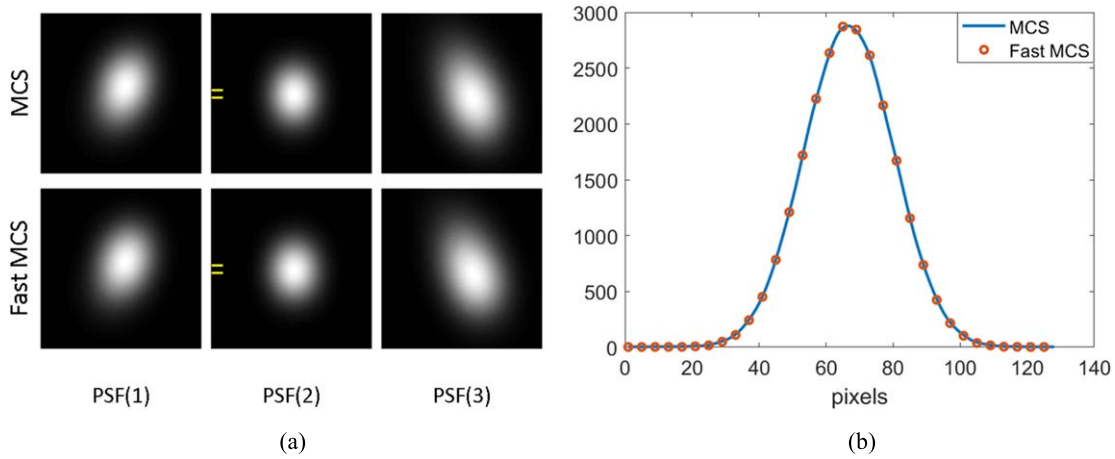


**Figure 5.** A comparison between full Monte-Carlo simulation and accelerated simulation of a point source scan with $^{99m}$Tc and the EXIRAD-3D collimator. (a) 2D PSF at three different locations on the detector. (b) 1D profiles through PSF(2) at the location indicated by yellow lines. For reference to the profiles from the traditional and ray-tracing methods, please see figure A1 in the appendix.

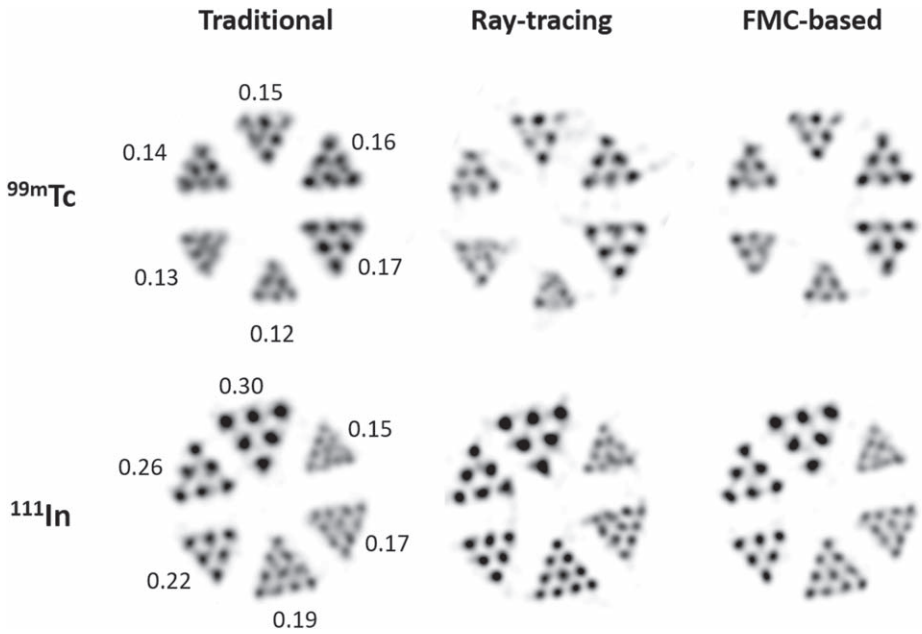


**Figure 6.** Experimental Derenzo phantom scans with $^{99m}$Tc and $^{111}$In with the EXIRAD-3D collimator to compare images resulting from the FMC-based matrices with those obtained with the reference matrices. The images were displayed with the iteration number and the filter size that maximise the CNR. Slice thicknesses were 0.2 mm and 0.8 mm for $^{99m}$Tc and $^{111}$In, respectively. Profiles through these images can be seen in figure A4 in the appendix.

voxel size (50 $\mu$m), and we experimentally observed that a large cut-off compensated for the effect of a too large point source size. Ideally, the point source should be smaller than the matrix voxel; however, making a tinier point source than 100 $\mu$m was difficult in our laboratory. Therefore, for the traditional matrices used in EXIRAD-3D experimental scans, we chose a matrix cut-off of 20% which resulted in higher-resolution images than a matrix cut-off of 4%, as shown in figure A2 in the appendix.

The ray-tracing code required energy-dependent attenuation coefficients of the collimator material ($\mu_c$) and of the detector crystal ($\mu_d$) (table 2). $\mu_c$ was obtained from Seltzer (1993), Hubbell and Seltzer (1995) and $\mu_d$ was calculated from MCS in the same way as in Nguyen *et al* (2020a). The ray-tracing code also required a collimator file which was either an analytical description or a voxelised volume. Generating a matrix with the analytical collimator require less computation time than with the voxelised collimator. The analytical description was sufficiently accurate for HE-UHR-M, while the voxelised volume was needed for EXIRAD-3D to model complex shielding layer that are difficult to be described analytically. The voxel size of the voxelised collimator should be small enough to avoid the discretisation effect of the pinholes (0.15 mm in diameter for EXIRAD-3D), but too small collimator voxels significantly increase the ray-tracing time. For this EXIRAD-3D collimator, the

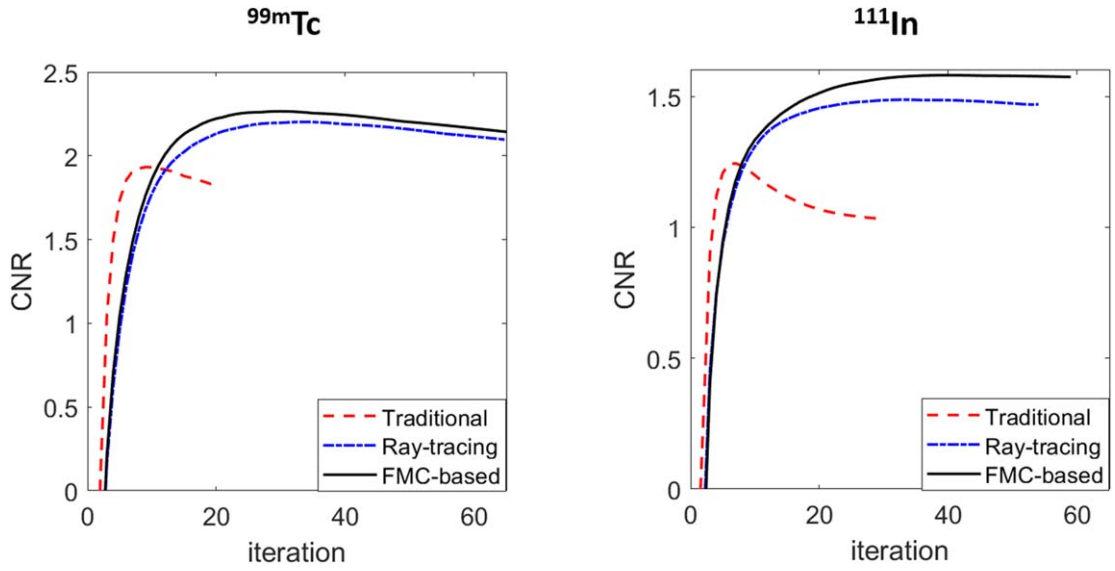


**Figure 7.** CNR comparison between the FMC-based matrices and the reference matrices for the experimental Derenzo phantom scans with $^{99m}$Tc and $^{111}$In. The traditional matrix used a >100 $\mu$m point source, while the FMC-based matrix used a ~0 $\mu$m point source.

**Table 3.** Chosen factor $c$ (used in equation (1)) and time required for point source simulations, comparing MCS and fast MCS. The listed time included the GATE simulation time and the time to generate raw PSFs from the GATE output files. Note that the acceleration was not applied for $^{90}$Y, as previously explained in section 2.3.2.

| | EXIRAD-3D | | | | HE-UHR-M |
|---|---|---|---|---|---|
| | $^{99m}$Tc | $^{123}$I | $^{111}$In | $^{67}$Ga | $^{90}$Y |
| $c$ | 3.0 | 3.0 | 5.0 | 5.0 | N/A |
| MCS | 34 h | 34 h | 42 h | 22 h | 59 h |
| Fast MCS | 32 min | 32 min | 61 min | 51 min | N/A |

**Table 4.** The time required to generate matrices with FMC-based method, traditional method, and ray-tracing method. For the FMC-based matrices, the time already included the FMCS time (table 3). The time to generate traditional matrices was the same for different radionuclides because these matrices only modelled photon transport at 140 keV.

| | EXIRAD-3D | | | | HE-UHR-M |
|---|---|---|---|---|---|
| | $^{99m}$Tc | $^{123}$I | $^{111}$In | $^{67}$Ga | $^{90}$Y |
| Traditional | 2.8 h | 2.8 h | 2.8 h | 2.8 h | 23 min |
| Ray-tracing | 11.7 d | 12.1 d | 13.0 d | 12.1 d | 1.6 d |
| FMC-based | 3.3 h | 3.4 h | 4.2 h | 6.3 h | 2.5 d |

finest voxel size that can be set was 0.025 mm which is still relatively coarse compared to the pinhole diameters (figure 4), but it was hard to reduce it further while keeping a feasible matrix calculation time.

## 3. Results

### 3.1. Validation of accelerated point source simulation

Figure 5 compares the accelerated point source simulation (FMCS) with the full MCS of a $^{99m}$Tc point source scan for EXIRAD-3D. The presented PSF corresponds to photons from a point source at the collimator's centre going through three different pinholes. Both the 2D PSFs and the 1D profiles indicate that the acceleration method for point source simulation produces the same PSFs as the full simulation does. This is true for PSFs with other point source positions. The normalised root mean squared error between PSFs from MCS and FMCS

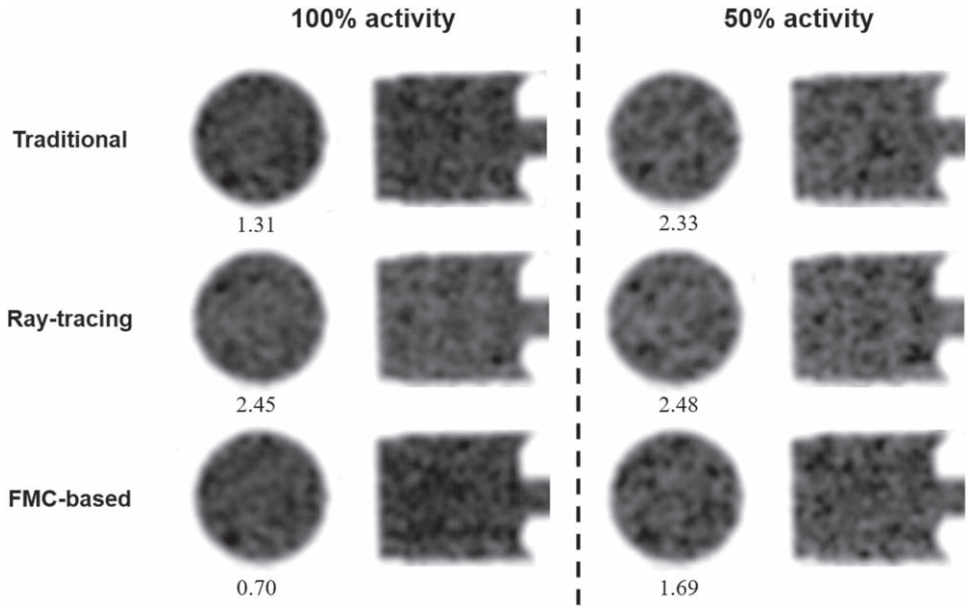


**Figure 8.** Experimental cylindrical phantom scan with $^{99m}$Tc to compare the FMC-based matrix with the reference matrices. The uniformity is listed under the image. The smaller this number, the better. Slice thickness was 0.2 mm.

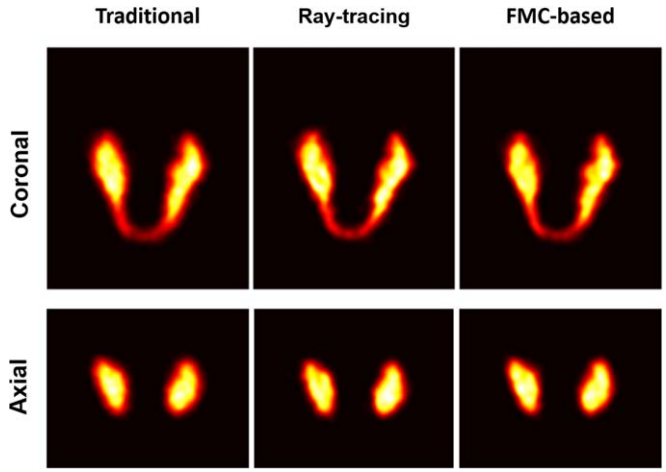


**Figure 9.** Experimental mouse thyroid scan with $^{123}$I to compare the FMC-based matrix with the reference matrices. Slice thickness was 0.2 mm.

is about $4.2 \times 10^{-4}$. Meanwhile, the accelerated version takes significantly less computation time compared to the full simulation, as summarised in table 3. In this table, the time for simulating a full set of PSFs for each of the studied FMC-based matrices in this work and the chosen factor $c$ as described in section 2.3.2 are reported. The timing was done on a Linux cluster with Intel(R) Xeon(R) CPUs E5-2620, and 250 cores were used in total.

### 3.2. Experimental $^{99m}$Tc and $^{111}$In phantom scans

Figure 6 presents the experimental results of the Derenzo phantom scans with $^{99m}$Tc and $^{111}$In. The traditional matrix yielded comparable image resolutions as the FMC-based matrix while showing a visually lower contrast between the hot rods and the background regions between the rods. This is probably because the point source used in the calibration scan was too large while ideally, the point source size should be smaller than the image voxel size, as illustrated in figure A1 and table A1. The ray-tracing matrix resulted in images with more background artefacts than the other matrices. We believe this is because the collimator voxel size of 0.025 mm was still not fine enough to represent the 0.15 mm diameter pinholes accurately (figure 4). It was hard to reduce this collimator voxel size further while still keeping a practical matrix generation time. Generating the ray-tracing matrix for EXIRAD-3D took about 11–13 d (table 4) on a Windows server with Intel® Xeon® CPU E5-2680 v3

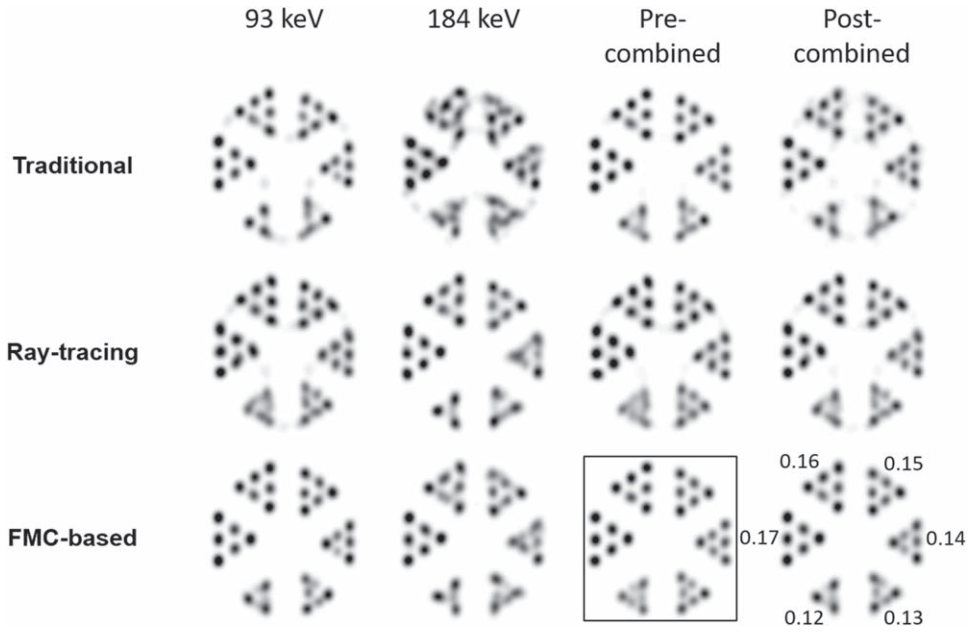


**Figure 10.** Simulated Derenzo phantom scan with $^{67}$Ga. The images were displayed with the iteration number and the filter size that maximise the CNR. The image with the highest CNR was highlighted in a box. Slice thickness was 0.8 mm. Profiles through these images can be seen in figure A4 in the appendix.

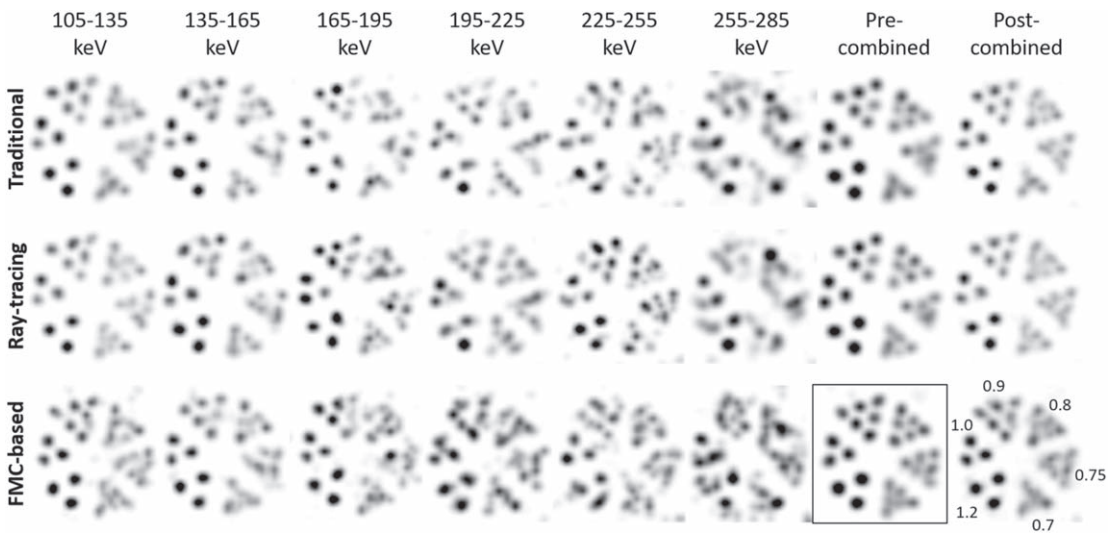


**Figure 11.** Simulated Derenzo phantom scan with $^{90}$Y. The ray-tracing matrix used an analytical collimator, so there was no problem of collimator voxelisation. The images were displayed with the iteration number and the filter size that maximise the CNR. The image with the highest CNR was highlighted in a box. Slice thickness was 2 mm. Profiles through these images can be seen in figure A4 in the appendix.

(48 cores) and was thus already impractically long. For both scans, the FMC-based matrices achieved higher CNRs than the traditional and ray-tracing matrices (figure 7). Table 4 also presents the time to generate matrices with different methods, showing that FMC-based method needed slightly more time than the traditional method and significantly less time than the ray-tracing method. Note that in case of $^{90}$Y, the ray-tracing method used an analytical description of the collimator instead of a voxelised volume; therefore, it was faster than the FMC method.

Figure 8 presents the experimental results of the uniform phantom scan with $^{99m}$Tc. For each scan, an axial slice and a coronal slice were shown, and the calculated uniformity measures were provided. Note that a lower number for this measure means better image uniformity. With each matrix, we observed that the obtained uniformity converges quickly after only a few iterations (figure A3 in the appendix). In all of the cases presented, the FMC-based matrix yielded the most uniform image among all matrices tested.

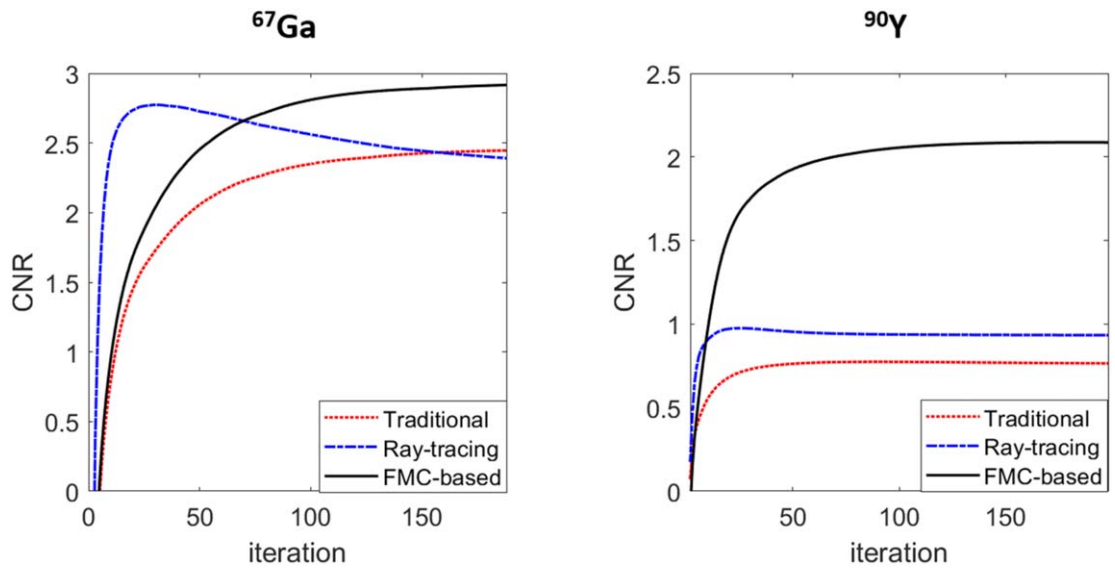


**Figure 12.** CNR comparison between the FMC-based matrices and the reference matrices for the simulated Derenzo phantom scans with $^{67}$Ga and $^{90}$Y. This figure only showed the best case for each matrix generation method (the pre-combined image). Both the traditional and FMC-based matrices for these simulated scans used a ~0 $\mu$m point source.

### 3.3. Experimental $^{123}$I mouse thyroid scan

Figure 9 shows images of the mouse thyroid reconstructed with the FMC-based matrix and the reference matrices. The images clearly visualised two thyroid lobes that are connected by a thin isthmus (see the coronal slices in figure 9). The isthmus was seen because it also had iodine uptake and its width of about 0.3 mm (Treuting and Dintzis 2012) can be well visualised due to the high-resolution of EXIRAD-3D. Among the matrices used, the traditional matrix resulted in a slightly more blurry image, especially when looking at the isthmus. The other matrices yielded visually almost similar images. Although there is no ground truth in this experiment to quantitatively compare the matrices' performance, we can conclude that the FMC-based matrix works with the real mouse tissue scan.

### 3.4. Simulated $^{67}$Ga scan: combining multiple photopeaks

Figure 10 compares the EXIRAD-3D $^{67}$Ga reconstructions with different matrices and several energy window settings. In all of the presented cases, the 93 keV photopeak produced images with clearer rods than the 184 keV photopeak. Post-reconstruction combining the images from separate energy windows did not show a clear advantage over only using the 93 keV photopeak. Pre-reconstruction combining the data and using a single matrix in reconstruction yielded the best image. The traditional matrix and ray-tracing matrix resulted in good images in the pre-combined case; however, with a little distortion in the 0.12–0.13 mm rod sectors. The FMC-based matrix performed better than the traditional and ray-tracing matrices by showing faithful shapes of the 0.13 mm rods, almost separating the rods in the 0.12 mm sector, and yielding the highest CNR (figure 12). With this $^{67}$Ga scan, a resolution of 0.13 mm was achieved.

### 3.5. Simulated $^{90}$Y scan: utilising a wide continuous energy spectrum

Figure 11 compares the HE-UHR-M $^{90}$Y reconstructions with different matrices and several energy window settings. The 105–135 keV energy window produced better images than the other single energy windows. This is understandable because more photons were detected within this window than in the other windows (figure 3). For all matrices, post-reconstruction combining the images from separate energy windows did not show a clear advantage over using the individual energy windows. Pre-reconstruction combining the data and using a single FMC-based matrix in reconstruction yielded the best image visually and also the highest CNR (figure 12). With this $^{90}$Y scan, a resolution of 0.75 mm was achieved.

## 4. Discussion

We have introduced an efficient and accurate Monte-Carlo based system matrix generation method for pinhole SPECT and validated it on our VECTor scanner with a HE-UHR-M collimator and an EXIRAD-3D collimator for a wide range of radionuclides. In the presented imaging situations, the FMC-based matrix demonstrates

advantages over the traditional and ray-tracing matrices. These advantages are mainly exhibited in two aspects. First, for very-high-resolution imaging, i.e. with EXIRAD-3D, the FMC-based matrix lessens the difficult task of fabricating a tiny point source, smaller than the image voxels (50 $\mu$m for EXIRAD-3D), as needed with the traditional matrix, and avoids extensive matrix computation time as with the ray-tracing matrix. Second, for imaging radionuclides with complex emission energy spectra such as $^{67}$Ga and $^{90}$Y, the FMC-based matrix offers a single matrix image reconstruction solution by modelling multiple photopeak windows or a wide continuous energy window into one matrix. With the ray-tracing method, it is in principal also possible to combine matrices from multiple energies into a single matrix by summing matrix elements for the corresponding voxel-to-pixel paths with certain weights that are proportional to the emission yields at different energies. However, it takes time to perform the same ray-tracing simulation for multiple energies, and it is hard to do this for the continuous emission spectrum of $^{90}$Y. In other cases, with systems having lower resolutions than the resolution that EXIRAD-3D offers, and with radionuclides emitting single energy spectra, the traditional or ray-tracing matrices are expected to be a good choice; however, the FMC-based matrix can be used as well. Therefore, the FMC-based matrix generation method can be a versatile system modelling method for pinhole SPECT systems.

The FMC-based matrix already models realistic image-degrading effects, such as positron range or beta-to-bremsstrahlung range, which are not always included in the traditional and ray-tracing matrices. In this work, we have not examined in depth all these effects and only shown the effect of modelling beta-to-bremsstrahlung range for $^{90}$Y. In this case, correcting the beta-to-bremsstrahlung range in the forward projection step of image reconstruction also worked with the traditional and ray-tracing matrices and the need for modelling it inside the matrix as with the FMC-based method was not clear. However, the proposed method is at least simpler than the traditional and ray-tracing methods in the sense that an additional effort to correct for these image-degrading effects is not needed.

MCS is usually computationally expensive; however, the point source simulation acting as the key step in the FMC-based system modelling procedure takes a relatively short time (less than 1 h for most of the cases in table 3) thanks to the used acceleration technique (section 2.3.2). Therefore, FMC-based matrix generation time is only slightly longer than the time required for making the traditional matrix and can be significantly shorter than the time required for calculating the ray-tracing matrix. For instance, generating a matrix for EXIRAD-3D and $^{99m}$Tc takes about 1.5 d with the FMC-based method or the traditional method, while it takes about 12 days with the ray-tracing method.

With the FMC-based system modelling, ideally, a new matrix needs to be generated when the radionuclide or the energy window setting changes. For a new radionuclide, the procedure needs to be restarted from the point source simulation step, but if only the energy window setting is adjusted for the same radionuclide, the point source simulation step does not need to be performed again. Besides, the PSF fitting step in the proposed method uses Gaussian functions, which work well in modelling PSFs for the studied energies ($\leqslant$285 keV). When imaging high-energy isotopes such as PET isotopes, because of more scatter and penetration occurring near the pinhole edges, more complex functions should be used.

## 5. Conclusion

This work presents a new FMC-based system modelling method for ultra-high-resolution pinhole SPECT. The results show that the proposed method is efficient, accurate, and versatile in creating energy-dependent system matrix for various radionuclides. It is more generalised than the traditional method when changing radionuclide or energy window setting, and more computationally efficient than the ray-tracing method for very-high-resolution systems such as EXIRAD-3D. The FMC-based method also shows the advantage of being able to combine energies in a single matrix.

## Acknowledgments

The authors would like to thank Sofia Koustoulidou for helping with the experimental scans, and Chris Kamphuis for helping with image reconstructions as well as giving insightful comments and discussions.

# Appendix

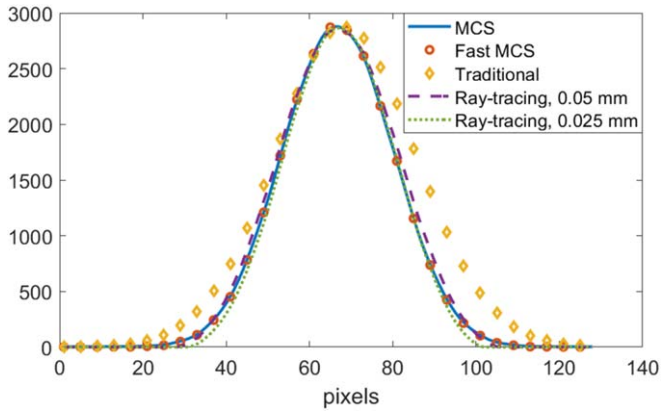


**Figure A1.** Profiles through a PSF location from a point source scan with $^{99m}$Tc and the EXIRAD-3D collimator. The results are from the MCS, the fast MCS, the traditional matrix, and the ray-tracing matrix. Note that the wide PSF with the traditional matrix is due to a too large point source used in the measurement. Two collimator voxel size were presented for the ray-tracing matrix.

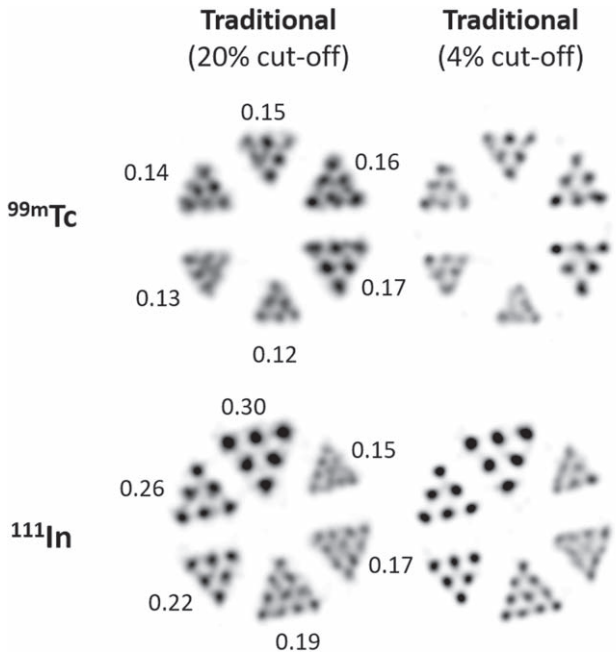


**Figure A2.** Experimental Derenzo phantom scans with $^{99m}$Tc and $^{111}$In with the EXIRAD-3D collimator to compare different cut-offs used for the tradition matrices. The images were displayed with the iteration number and the filter size that maximise the CNR. Slice thicknesses were 0.2 mm and 0.8 mm for $^{99m}$Tc and $^{111}$In, respectively. For both radionuclides, the traditional matrix with 20% cut-off yielded images that resolve smaller rods than the traditional matrix with 4% cut-off. We believe this is because a higher cut-off compensates for the point source size (>100 $\mu$m diameter) used for calibration that could not be made smaller than the image voxel size (50 $\mu$m). This is also demonstrated in table A1 which shows the effect of the point source size.

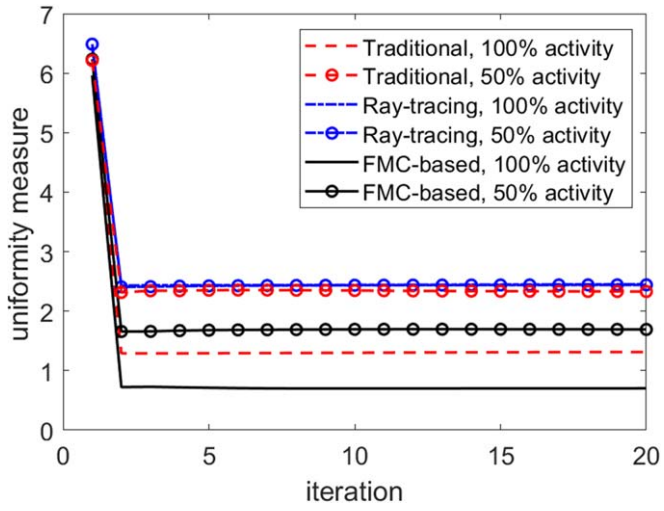


**Figure A3.** Uniformity versus iteration number for the experimental cylindrical phantom scan with $^{99m}$Tc showed in figure 8, comparing the FMC-based matrix with the reference matrices. A smaller number means a better uniformity.

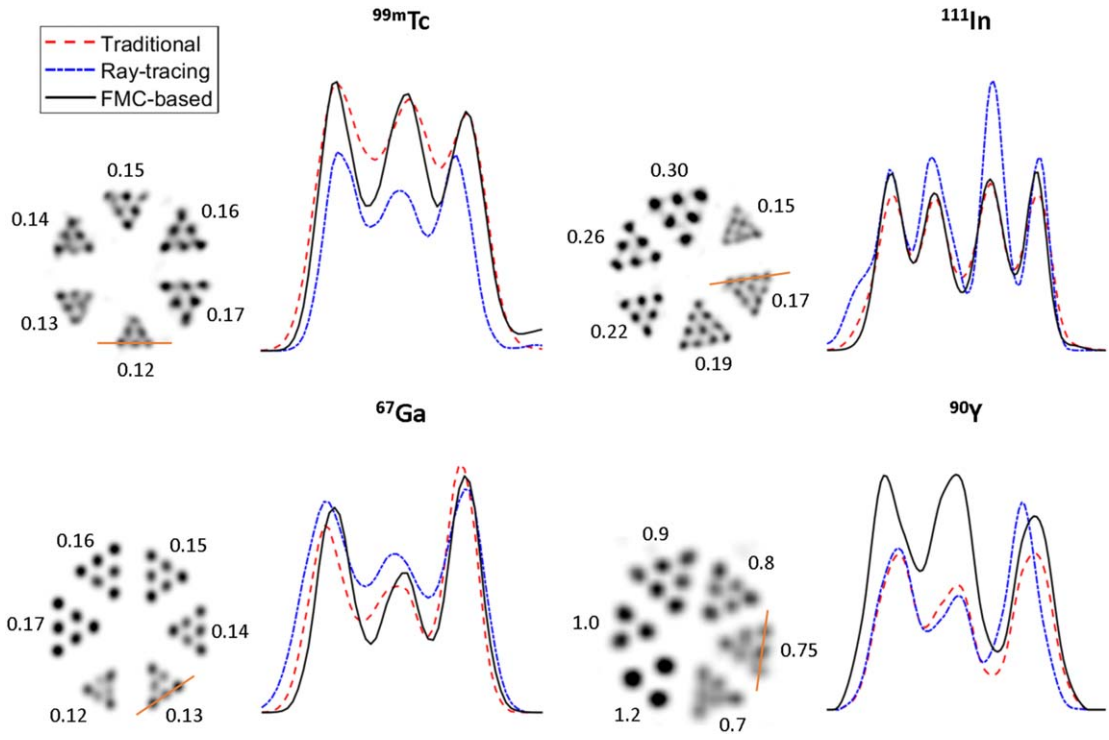


**Figure A4.** Profiles obtained from the best reconstructed Derenzo phantom image (highest CNR) in figures 6, 10, and 11 for each matrix generation method. Locations of the profile is indicated with a line drawn on the smallest discernible rod sector in each case. The rod diameters are shown in mm.

**Table A1.** Effect of the size of the point source used in calibration measurement on the reconstruction of the Derenzo phantom scan with $^{99m}$Tc. The listed CNR is the highest that was achieved with the optimal iteration number and filter size. The real fabricated point source had a diameter of >100 $\mu$m, while the diameter of the simulated point source in GATE was easily adjusted to 100 and ~0 $\mu$m (an exact point).

| Traditional | | FMC-based | |
|---|---|---|---|
| PS >100 $\mu$m | PS >100 $\mu$m | PS 100 $\mu$m | PS ~0 $\mu$m |
| 20% cut-off | 4% cut-off | 4% cut-off | 4% cut-off |
| **CNR = 1.93** | **CNR = 1.55** | **CNR = 1.75** | **CNR = 2.27** |

## ORCID iDs

Minh Phuong Nguyen https://orcid.org/0000-0001-6114-5682

## References


Aguiar P, Pino F, Silva-Rodríguez J, Pavía J, Ros D, Ruibal Á and El Bitar Z 2014 Analytical, experimental, and Monte Carlo system response matrix for pinhole SPECT reconstruction *Med. Phys.* **41** 032501

Auer B, Zeraatkar N, Banerjee S, Goding J C, Furenlid L R and King M A 2018 Preliminary investigation of a Monte Carlo-based system matrix approach for quantitative clinical brain 123I SPECT imaging *2018 IEEE Nuclear Science Symp. and Medical Imaging Conf., NSS/MIC 2018—Proc. (Sydney, NSW, 10–17 November 2018)* (Piscataway, NJ: IEEE) pp 1–2

Beekman F J, van der Have F, Vastenhouw B, Van der Linden A J A, Van Rijk P P, Burbach J P H and Smidt M P 2005 U-SPECT-I: a novel system for submillimeter-resolution tomography with radiolabeled molecules in mice *J. Nucl. Med.* **46** 1194–200 https://pubmed.ncbi.nlm.nih.gov/16000289/

Beenhouwer J D and Staelens S 2010 Fast GATE multi-pinhole SPECT simulations *IEEE Nucl. Sci. Symp. Med. Imaging Conf. (Knoxville, TN, 30 October–6 November 2010)* (Piscataway, NJ: IEEE) pp 3634–7

Bitar Z E, Bekaert V and Brasse D 2011 Using Monte Carlo based system matrix for increasing detection efficiency in small animal SPECT *2011 IEEE Nuclear Science Symp. Conf. Record (Valencia, Spain, 23–29 Octpber 2011)* (Piscataway, NJ: IEEE) pp 4390–2

Bitar Z E, Pino F, Candela C, Ros D, Pavía J, Rannou F R, Ruibal A and Aguiar P 2014 The performance of a hybrid analytical-Monte Carlo system response matrix in pinhole SPECT reconstruction *Phys. Med. Biol.* **59**

Chu S Y F, Ekstrom L P and Firestone R B 1998 Table of Radioactive Isotopes http://nucleardata.nuclear.lu.se/toi/nucSearch.asp

Chun S Y, Nguyen M P, Phan T Q, Kim H, Fessler J A and Dewaraja Y K 2020 Algorithms and analyses for joint spectral image reconstruction in Y-90 bremsstrahlung SPECT *IEEE Trans. Med. Imaging* **39** 1369–79

Dewaraja Y K, Chun S Y, Srinivasa R N, Kaza R K, Cuneo K C, Majdalany B S, Novelli P M, Ljungberg M and Fessler J A 2017 Improved quantitative $^{90}$Y bremsstrahlung SPECT/CT reconstruction with Monte Carlo scatter modeling *Med. Phys.* **44** 6364–76

Elschot M, Lam M G E H, van den Bosch M A A J, Viergever M A and de Jong H W A M 2013 Quantitative Monte Carlo-based 90Y SPECT reconstruction *J. Nucl. Med.* **54** 1557–63

Feng B, Chen M, Bai B, Smith A M, Austin D W, Mintzer R A, Osborne D and Gregor J 2010 Modeling of the point spread function by numerical calculations in single-pinhole and multipinhole spect reconstruction *IEEE Trans. Nucl. Sci.* **57** 173–80

Furenlid L R, Wilson D W, Chen Y-C, Kim H, Pietraski P J, Crawford M J and Barrett H H 2004 FastSPECT II: a second-generation high-resolution dynamic SPECT imager *IEEE Trans. Nucl. Sci.* **51** 631–5

Gieles M, de Jong H W A M and Beekman F J 2002 Monte Carlo simulations of pinhole imaging accelerated by kernel-based forced detection *Phys. Med. Biol.* **47** 1853–67

Goorden M C and Beekman F J 2010 High-resolution tomography of positron emitters with clustered pinhole SPECT *Phys. Med. Biol.* **55** 1265–77

Goorden M C, van der Have F, Kreuger R, Ramakers R M, Vastenhouw B, Burbach J P H, Booij J, Molthoff C F M and Beekman F J 2013 VECTor: a preclinical imaging system for simultaneous submillimeter SPECT and PET *J. Nucl. Med.* **54** 306–12

Goorden M C, Kamphuis C, Ramakers R M and Beekman F J 2020 Accelerated image reconstruction by a combined dual-matrix dual-voxel approach *Phys. Med. Biol.* **65** 105014

Goorden M C, van Roosmalen J, van der Have F and Beekman F J 2016 Optimizing modelling in iterative image reconstruction for preclinical pinhole PET *Phys. Med. Biol.* **61** 3712–33

Hesterman J Y, Kupinski M A, Furenlid L R, Wilson D W and Barrett H H 2007 The multi-module, multi-resolution system (M3R): a novel small-animal SPECT system *Med. Phys.* **34** 987–93

Hubbell J H and Seltzer S M 1995 Tables of x-ray mass attenuation coefficients and mass energy-absorption coefficients http://physics.nist.gov/PhysRefData/XrayMassCoef/cover.html

Hutton B F, Hudson H M and Beekman F J 1997 A clinical perspective of accelerated statistical reconstruction *Eur. J. Nucl. Med.* **24** 797–808

Ishii S, Shishido F, Miyajima M, Sakuma K, Shigihara T and Kikuchi K 2011 Whole-body gallium-67 scintigraphic findings in igg4-related disease *Clin. Nucl. Med.* **36** 542–5

Jan S *et al* 2011 GATE V6: a major enhancement of the GATE simulation platform enabling modelling of CT and radiotherapy *Phys. Med. Biol.* **56** 881–901

Jan S *et al* 2004 GATE: a simulation toolkit for PET and SPECT *Phys. Med. Biol.* **49** 4543–61

Kennedy A 2014 Radioembolisation of hepatic tumors *J. Gastrointest. Oncol.* **5** 178–89

Kostakoglu L, Leonard J P, Kuji I, Coleman M, Vallabhajosula S and Goldsmith S J 2002 Comparison of fluorine-18 fluorodeoxyglucose positron emission tomography and Ga-67 scintigraphy in evaluation of lymphoma *Cancer* **94** 879–88

Lhommel R, Van Elmbt L, Goffette P, Van Den Eynde M, Jamar F, Pauwels S and Walrand S 2010 Feasibility of 90Y TOF PET-based dosimetry in liver metastasis therapy using SIR-Spheres *Eur. J. Nucl. Med. Mol. Imaging* **37** 1654–62

Liu Z, Kastis G A, Stevenson G D, Barrett H H, Furenlid L R, Kupinski M A, Patton D D and Wilson D W 2002 Quantitative analysis of acute myocardial infarct in rat hearts with ischemia-reperfusion using a high-resolution stationary SPECT system *J. Nucl. Med.* **43** 933–9

Miller B W, Van Holen R, Barrett H H and Furenlid L R 2012 A system calibration and fast iterative reconstruction method for next-generation SPECT imagers *IEEE Trans. Nucl. Sci.* **59** 1990–6

Moore S C, Fakhri G E, Park M A and Kijewski M F 2003 Quantitative Ga-67 SPECT imaging *IEEE Nucl. Sci. Symp. Conf. Record* vol 4 *(Portland, OR, 19–25 October 2003)* (Piscataway, NJ: IEEE) pp 2898–900

Nowosinska E, Navalkissoor S, Quigley A and Buscombe J 2015 Is there a role for gallium-67 citrate SPECT/CT, in patients with renal impairment or who are renal transplant recipients, in identifying and localising suspected infection? *World J. Nucl. Med.* **14** 184–8

Nguyen M P, Goorden M C and Beekman F J 2020a EXIRAD-HE: multi-pinhole high-resolution *ex vivo* imaging of high-energy isotopes *Phys. Med. Biol.* **65** 225029

Nguyen M P, Goorden M C, Kamphuis C and Beekman F J 2019 Evaluation of pinhole collimator materials for micron-resolution *ex vivo* SPECT *Phys. Med. Biol.* **64** 105017

Nguyen M P, Ramakers R M, Kamphuis C, Koustoulidou S, Goorden M C and Beekman F J 2020b EXIRAD-3D: fast automated three-dimensional autoradiography *Nucl. Med. Biol.* **86–87** 59–65

Qi J and Leahy R M 2006 Iterative reconstruction techniques in emission computed tomography *Phys. Med. Biol.* **51** R541–78

Rong X, Du Y, Ljungberg M, Rault E, Vandenberghe S and Frey E C 2012 Development and evaluation of an improved quantitative 90Y bremsstrahlung SPECT method *Med. Phys.* **39** 2346–58

Seabold J E, Palestro C J, Brown M L, Datz F L, Forstrom L A, Greenspan B S, McAfee J G, Schauwecker D S and Royal H D 1997 Procedure guideline for gallium scintigraphy in inflammation. Society of nuclear medicine *J. Nucl. Med.* **38** 994–7

Seltzer S M 1993 Calculation of photon mass energy-transfer and mass energy-absorption coefficients *Radiat. Res.* **136** 147–70

Shirmohammad M 2016 *Ga-67 Imaging with Vector* University of British Columbia, Canada https://open.library.ubc.ca/cIRcle/collections/ubctheses/24/items/1.0319327

Siman W, Mikell J K and Kappadath S C 2016 Practical reconstruction protocol for quantitative $^{90}$Y bremsstrahlung SPECT/CT *Med. Phys.* **43** 5093–103

Szlávecz A, Hesz G and Benyó B 2019 The use of multi-energy photon emitters in 3D SPECT reconstruction *Biomed. Signal Process. Control* **47** 413–23

Taki J 1990 Cardiac sarcoidosis demonstrated by Tl-201 and Ga-67 SPECT Imaging *Clin. Nucl. Med.* **15** 636–39

Treuting P M and Dintzis S M 2012 *Comparative Anatomy and Histology: A Mouse and Human Atlas* (New York: Academic)

van Bommel E F H, Siemes C, van der Veer S J, Han S H, Huiskes A W L C and Hendriksz T R 2007 Clinical value of gallium-67 SPECT scintigraphy in the diagnostic and therapeutic evaluation of retroperitoneal fibrosis: a prospective study *J. Intern. Med.* **262** 224–34

van der Have F, Vastenhouw B, Ramakers R M, Branderhorst W, Krah J O, Ji C, Staelens S G and Beekman F J 2009 U-SPECT-II: an ultra-high-resolution device for molecular small-animal imaging *J. Nucl. Med.* **50** 599–605

van der Have F, Vastenhouw B, Rentmeester M and Beekman F J 2008 System calibration and statistical image reconstruction for ultra-high resolution stationary pinhole SPECT *IEEE Trans. Med. Imaging* **27** 960–71

Van Oosterom A and Strackee J 1983 The solid angle of a plane triangle *IEEE Trans. Biomed. Eng.* **BME-30** 125–6

Vaissier P E B, Beekman F J and Goorden M C 2016 Similarity-regulation of OS-EM for accelerated SPECT reconstruction *Phys. Med. Biol.* **61** 4300–15

Walker M D, Goorden M C, Dinelle K, Ramakers R M, Blinder S, Shirmohammad M, van der Have F, Beekman F J and Sossi V 2014 Performance assessment of a preclinical PET scanner with pinhole collimation by comparison to a coincidence-based small-animal PET scanner *J. Nucl. Med.* **55** 1368–74

Wu C, Van Der Have F, Vastenhouw B, Dierckx R A J O, Paans A M J and Beekman F J 2010 Absolute quantitative total-body small-animal SPECT with focusing pinholes *Eur. J. Nucl. Med. Mol. Imaging* **37** 2127–35

Wu C, De Jong J R, Gratama Van Andel H A, Van Der Have F, Vastenhouw B, Laverman P, Boerman O C, Dierckx R A J O and Beekman F J 2011 Quantitative multi-pinhole small-animal SPECT: uniform versus non-uniform chang attenuation correction *Phys. Med. Biol.* **56** 183–93